

UCLA

UCLA Previously Published Works

Title

Accelerated five-dimensional echo planar J-resolved spectroscopic imaging: Implementation and pilot validation in human brain

Permalink

<https://escholarship.org/uc/item/3b48h6z9>

Journal

Magnetic Resonance in Medicine, 75(1)

ISSN

0740-3194

Authors

Wilson, Neil E
Iqbal, Zohaib
Burns, Brian L
[et al.](#)

Publication Date

2016

DOI

10.1002/mrm.25605

Peer reviewed

Accelerated Five-Dimensional Echo Planar J-Resolved Spectroscopic Imaging: Implementation and Pilot Validation in Human Brain

Neil E. Wilson,¹ Zohaib Iqbal,¹ Brian L. Burns,¹ Margaret Keller,² and M. Albert Thomas^{1*}

Purpose: To implement an accelerated five-dimensional (5D) echo-planar J-resolved spectroscopic imaging sequence combining 3 spatial and 2 spectral encoding dimensions and to apply the sequence in human brain.

Methods: An echo planar readout was used to acquire a single spatial and a single spectral dimension during one readout. Nonuniform sampling was applied to the two phase-encoded spatial directions and the indirect spectral dimension. Nonlinear reconstruction was used to minimize the ℓ_1 -norm or the total variation and included a spectral mask to enhance sparsity. Retrospective reconstructions at multiple undersamplings were performed in phantom. Ten healthy volunteers were scanned with 8× undersampling and compared to a fully sampled single slice scan.

Results: Retrospective reconstruction of fully sampled phantom data showed excellent quality at 4×, 8×, 12×, and 16× undersampling using either reconstruction method. Reconstruction of prospectively acquired in vivo scans with 8× undersampling showed excellent quality in the occipitoparietal lobes and good quality in the frontal lobe, consistent with the fully sampled single slice scan.

Conclusion: By utilizing nonuniform sampling with nonlinear reconstruction, 2D J-resolved spectra can be acquired over a 3D spatial volume with a total scan time of 20 min, which is reasonable for in vivo studies. **Magn Reson Med 000:000–000, 2015.** © 2015 Wiley Periodicals, Inc.

Key words: echo-planar J-resolved spectroscopic imaging; compressed sensing; nonuniform sampling; J-resolved spectroscopic imaging; human brain; 3D spectroscopic imaging

INTRODUCTION

Spectroscopic imaging (SI) allows the acquisition of spatially mapped spectra over two or three dimensions (1). Compared to single voxel techniques, SI offers much

larger spatial coverage and better resolution as well as the ability to discriminate spectra at different locations. SI can be an important tool for mapping the spatial extent of diseased tissue as underlying metabolic changes can occur before any visible anatomic variation.

The scan time for classical SI sequences is proportional to the number of phase encoding increments and therefore increases with the resolution and number of dimensions. Mansfield proposed using an echo planar readout to interleave the collection of one of the spatial dimensions along with the directly acquired spectral dimension (2). This type of spatial-spectral readout has been applied in vivo with the originally-proposed Cartesian k-space trajectory (3) as well as with spiral-based (4) and concentric circular-based trajectories (5).

A major issue with proton (1H) spectroscopy in the human brain is that nearly all of the measurable resonances lie in a relatively small bandwidth covering approximately 4 ppm, resulting in spectra that suffer from severe overlap and crowding. Spectral dispersion can be increased using two-dimensional (2D) MR Spectroscopy (6). Localized versions of some of the simpler 2D MR Spectroscopy sequences have been applied in single voxel techniques in vivo (7–9). In particular, localized J-resolved spectroscopy (JPRESS) (7) is achieved by adding incremental delays symmetrically around the last refocusing pulse in a PRESS (10) localization. At each increment, the chemical shift is refocused at readout. However, scalar coupling is not refocused by a 180° pulse and therefore, evolves differently for each increment. 2D Fourier transformation of the time domain data results in a spectrum in which peak splitting of coupled metabolites is in a separate dimension from the chemical shift.

Multidimensional SI refers to SI scans that collect two spectral dimensions, such as with J-resolved (11) or correlated spectroscopy (12,13). The additional information present in the second spectral dimension comes at the expense of greatly increased scan time, limiting the application of multidimensional SI to relatively low resolution single slice acquisitions even with an echo planar readout.

Techniques used to accelerate MRI such as partial Fourier acquisition (14) or parallel imaging (15,16) have been applied to acquire fewer phase encoding steps in SI as well (17–20). However, the potential acceleration is limited for low resolution SI, and these methods do not accelerate the acquisition of the indirect spectral dimension.

¹Department of Radiological Sciences, University of California, Los Angeles, California, USA.

²Department of Pediatrics, University of California, Los Angeles, California, USA

Grant sponsor: National Institute of Health; Grant number: #5R21NS080649-02; Grant sponsor: CDMRP Prostate and Breast Cancer Research Programs; Grant number: PCRP#W81XWH-11-1-0248 and BCRP#W81XWH-10-1-0743.

*Correspondence to: M. Albert Thomas; Ph.D., Department of Radiological Sciences, University of California Los Angeles, CA. E-mail: athomas@mednet.ucla.edu, Twitter handle: @mathomas95

Received 17 September 2014; revised 29 November 2014; accepted 12 December 2014

DOI 10.1002/mrm.25605

Published online 00 Month 2015 in Wiley Online Library (wileyonlinelibrary.com).

Alternatively, nonuniform sampling (NUS) with compressed sensing (CS) reconstruction offers greater potential acceleration as the undersampling can be spread over multiple dimensions (21). Hu et al. used a blipped phase encode during readout to nonuniformly sample the spatial and spectral dimensions in hyperpolarized C-13 SI (22). Our group has previously shown the potential for 4-fold acceleration of single-slice echo-planar J-resolved SI by undersampling the (k_y, t_1) plane (23).

Here, we extend those principles to 5D (3 spatial + 2 spectral) SI and apply NUS to the (k_y, k_z, t_1) volume. The third spatial dimension can provide nearly full coverage of the brain in a single scan. This aspect is critical when locations of interest (e.g., tumors) are not apparent in an MRI scan or require detailed mapping in three dimensions (24). In addition, regional metabolite differences have been found from whole brain SI in varied pathologies such as traumatic brain injury (25) and amyotrophic lateral sclerosis (26,27). The third spatial dimension also enhances the self sparsity of data, and spreading the undersampling over an additional dimension increases the incoherence of the artifacts (21). These factors improve the performance of CS reconstruction and allow us to acquire data with an 8-fold acceleration, which is the same time required for a fully sampled single-slice data set at the resolution shown here. It should be mentioned that previous applications of CS to SI were used to accelerate already existing protocols, whereas in our case, 5D SI is untenable in vivo without significant acceleration.

Existing fast 3D SI methods all acquire data with a single spectral dimension and have typically focused on high resolution mapping of the singlet signals of NAA, creatine, and choline (20,28,29). Dreher et al. used a steady-state free precession EPSI to additionally map myo-inositol, though their technique is not well suited for detecting glutamate/glutamine (Glx) resonances (30). Recently, reliable short TE whole brain maps of Glx were also shown (31). However, none of these techniques offer much potential for separately resolving highly overlapped metabolites such as glutamate and glutamine.

METHODS

Phantom

All scans were acquired on a Siemens 3T Trio scanner, with TR/minimum TE = 1200/30 ms. A phantom with physiological concentrations (32) of 16 grey matter brain metabolites was scanned 12 times to measure spectral quality and reproducibility. The fully sampled 5D echo planar-J-resolved SI sequence acquired a k-space volume with 16 points in the readout direction (k_x) and 16 and 8 points in the two phase encoding directions (k_y and k_z , respectively). The field of view (FOV) was $16 \times 16 \times 12$ cm³. Each k_x line was repeatedly acquired for 256 t_2 points per TR, and 64 TE increments (t_1 points) were acquired. A maximum echo sampling scheme was applied in which t_1 is incremented only before the last refocusing pulse (33,34). The second increment that leads to refocused chemical shift is applied as a frequency-dependent, linear phase correction in post-processing for each acquisition. The reconstructed bandwidths in the direct (F_2) and indirect (F_1) spectral

dimensions were 1190 and 500 Hz, respectively. Water suppression was applied before each scan (35). Scans were recorded with a single channel transmit/receive extremity coil mostly, though three scans were recorded with the same head receive coil used in the in vivo experiments. Total scan time was 2 h 44 min. Different NUS rates were applied retrospectively.

In Vivo

Ten healthy volunteers (mean age 25.0 years old) were scanned using the same parameters as the phantom scans except that the FOV was increased to $24 \times 24 \times 16$ cm³, and $8 \times$ NUS was prospectively applied for a scan time of around 20 min. Outer volume saturation bands were included outside the PRESS volume of interest. An eight channel head receive coil was used. One scan was excluded due to poor water suppression as a result of subject motion. For a time-equivalent comparison, a fully sampled 4D single slice scan with the same slice thickness and in-plane resolution was also acquired in one healthy 23-year-old volunteer.

NUS Masks

Incoherent aliasing was achieved by randomly undersampling the (k_y, k_z, t_1) volume. As previously described in Ref. 23, a NUS density function that favors the higher SNR data points was considered and was given by

$$\rho(k_y, k_z, t_1) = \exp \left\{ -\frac{|k_y|}{a} - \frac{|k_z|}{b} - \frac{t_1}{c} \right\} \quad [1]$$

where $\rho(k_y, k_z, t_1)$ is the probability of sampling point (k_y, k_z, t_1) , $k_y \in \{-8, -7, \dots, 7\}$, $k_z \in \{-4, -3, \dots, 3\}$, $t_1 \in \{0, 1, \dots, 63\}$, and a , b , and c give the relative decay in each dimension. This method is similar in principle and motivation to that described by Barna et al. (36). In the 5D echo planar-J-resolved SI sequence as described above, there is less sampling in the spatial dimensions than the indirect spectral dimension, so to ensure adequate sampling of that indirect spectral dimension, we have set $a = b = 2$ and $c = 1$. The $8 \times$ mask used in phantom retrospectively and in vivo prospectively is shown in Figure 1. Independent masks were generated for $4 \times$, $8 \times$, $12 \times$, and $16 \times$ undersampling. In each case, 50 masks were generated offline, and the one with the smallest maximum off center peak of the point spread function was implemented on the scanner.

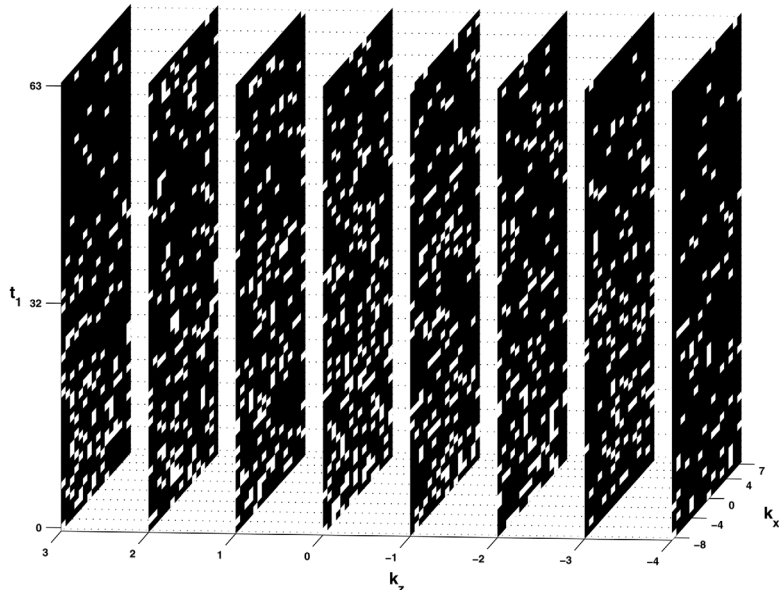
Reconstruction

Two versions of the CS reconstruction problem were formulated. In the first, the reconstructed data is considered self sparse, due largely to the sparsity of 2D JPRESS spectra, and the optimization is written as

$$\min_u \|u\|_1 \quad \text{s.t.} \|RFu - f\|_2^2 < \sigma^2 \quad [2]$$

where $u = u(x, y, z, F_2, F_1)$ is the reconstructed data, $f = f(x, k_y, k_z, F_2, t_1)$ is the undersampled data Fourier transformed across the fully sampled dimensions, σ^2 is an estimate of the noise variance of the sampled data

FIG. 1. $8\times$ NUS mask over the (k_y, k_z, t_1) volume used for phantom and in vivo scans. White squares indicate sampled points.



divided by 100, R is the NUS masking operator, and \mathcal{F} is the Fourier transform operator across the undersampled dimensions only. The objective function is the ℓ_1 -norm of the reconstructed data, and the constraint expresses data consistency through the ℓ_2 -norm of the difference between the acquired data and the subsampled reconstructed data. Each iteration of the solver requires transformation from the f domain to the u domain and back. For such large datasets and with a high number of iterations, a significant amount of reconstruction time is spent on Fourier transforms. Transforming the (k_x, t_2) dimensions only once before reconstruction therefore saves time and is permissible since $\mathcal{F}^{-1}R\mathcal{F}$ equals identity when the dimension is fully sampled ($R = \mathbf{1}$).

The second CS reconstruction is based on the assumption of piecewise constant spatial profiles and seeks to minimize the total variation (TV) of the reconstructed data with the same data consistency constraint. It is given by

$$\min_u \text{TV}(u) \quad \text{s.t.} \|\mathcal{R}\mathcal{F}u - f\|_2^2 < \sigma^2 \quad [3]$$

and was similar to the method used in Ref. 23. The TV-norm was given isotropically as

$$\text{TV}(u) = \sum_{i=1}^N \sqrt{(\nabla_x u)^2 + (\nabla_y u)^2 + (\nabla_z u)^2} \quad [4]$$

where N is the number of acquired data points. In this experiment, this problem took about three times longer per iteration than that of Eq. (2).

Both Eqs. (2) and (3) were solved using the split Bregman algorithm (37). The split Bregman algorithm seeks to minimize the Bregman distance of the objective function and uses operator splitting (38) to simplify the computations. It is equivalent to the alternating direction method of multipliers with one iteration (39). Each reconstruction had the same stopping criteria, namely: (1) a maximum number of 200 iterations and (2)

accepted level of deviation from the acquired data as expressed through the parameter σ .

Additional Processing

After Fourier transformation across t_2 but before reconstruction, a linear phase correction was applied to effectively refocus chemical shift as described above. At the same time, a spectral mask was applied in F_2 to select only the region between 1.2 and 4.3 ppm, which is where nearly all of the brain metabolites resonate. This constrains the dynamic range of the data and effectively removes the large residual water signal and most lipid contamination. A similar approach was applied by Eslami and Jacob to SI data with one spectral dimension (40).

The reconstruction was performed over each coil separately, and the individual coil reconstructions were combined as a sum-of-squares. Metabolite maps were found by integrating the reconstructed spectra over the peak ranges given in Table 1. An average noise power for each sized region was subtracted from the integral to compensate for the bias introduced by nonzero mean noise in the absolute magnitude spectra (41).

For the quantitative comparison, voxels were excluded based on any of three criteria: (1) low SNR, (2) undue influence of the residual water tail, and (3) large fat signal bleed. The spectral regions used to perform these tests are also given in Table 1. The first condition effectively excluded voxels outside the volume of interest, while the second was important for voxels in the frontal lobe. The third condition is important for voxels near the skull marrow. Acceptance criteria were manually confirmed with visual inspection of the NAA, Cr, and tCho singlets.

RESULTS

Phantom

Spectra from a central voxel in a typical phantom scan are shown with various retrospective undersamplings in

Table 1
Spectral Ranges Used to Measure Peak Integrals

	F_2 (ppm)	F_1 (Hz)
NAA	(1.8, 2.2)	(-15, 15)
Glx	(2.2, 2.6)	(-15, 15)
Cr30	(2.9, 3.1)	(-15, 15)
Cho	(3.1, 3.3)	(-15, 15)
ml	(3.4, 3.8)	(-15, 15)
Cr39	(3.8, 4.0)	(-15, 15)
Wat	(4.0, 4.3)	(-15, 15)
Tail	(2.0, 4.3)	(-250, 47)
Fat	(0.7, 1.6)	(-15, 15)
Sig	(2.4, 3.1)	(-15, 15)
Noise	(1.3, 2.5)	(120, 240)

Cho is total choline; Cr30 is the creatine singlet at 3.0 ppm; Cr39 is the creatine singlet at 3.9 ppm; Glx is glutamate and glutamine combined; ml is myo-inositol; NAA is N-acetylaspartate. Wat and Tail are used as a measure of baseline effects due to residual water contamination. Fat is a marker of lipid signal bleed. Sig is a marker of overall signal level. Noise is taken from a region that is devoid of any signal, desired or nuisance.

Figure 2 along with the same fully sampled spectrum. The minimum energy reconstruction in which the unacquired data points are filled in with zeros is shown (Fig. 2b) for the same $4\times$ undersampling as that reconstructed in Figure 2c with Eq. (2). Note that the spectral aliasing artifacts appear tilted along the F_1 dimension due to the maximum echo sampling scheme and postprocessing. The CS reconstructed $4\times$ spectra show excellent spectral quality with respect to the fully sampled. As expected, a decrease in spectral quality exemplified by residual aliasing and the removal of low lying peaks is observed with progressively larger undersampling. A metabolite map of the integrated volume of the NAA singlet is shown in Supporting Information Figure S1, showing the spatial aliasing artifacts in the minimum energy reconstruction in both the y - and z -directions. Metabolite maps for the remaining metabolites show similar quality.

Figure 3 shows the metabolite maps of Glx from the same phantom scan reconstructed using TV minimization in Eq. (3) undersampled by 8, 12, and 16, along with the fully sampled reconstruction. For each

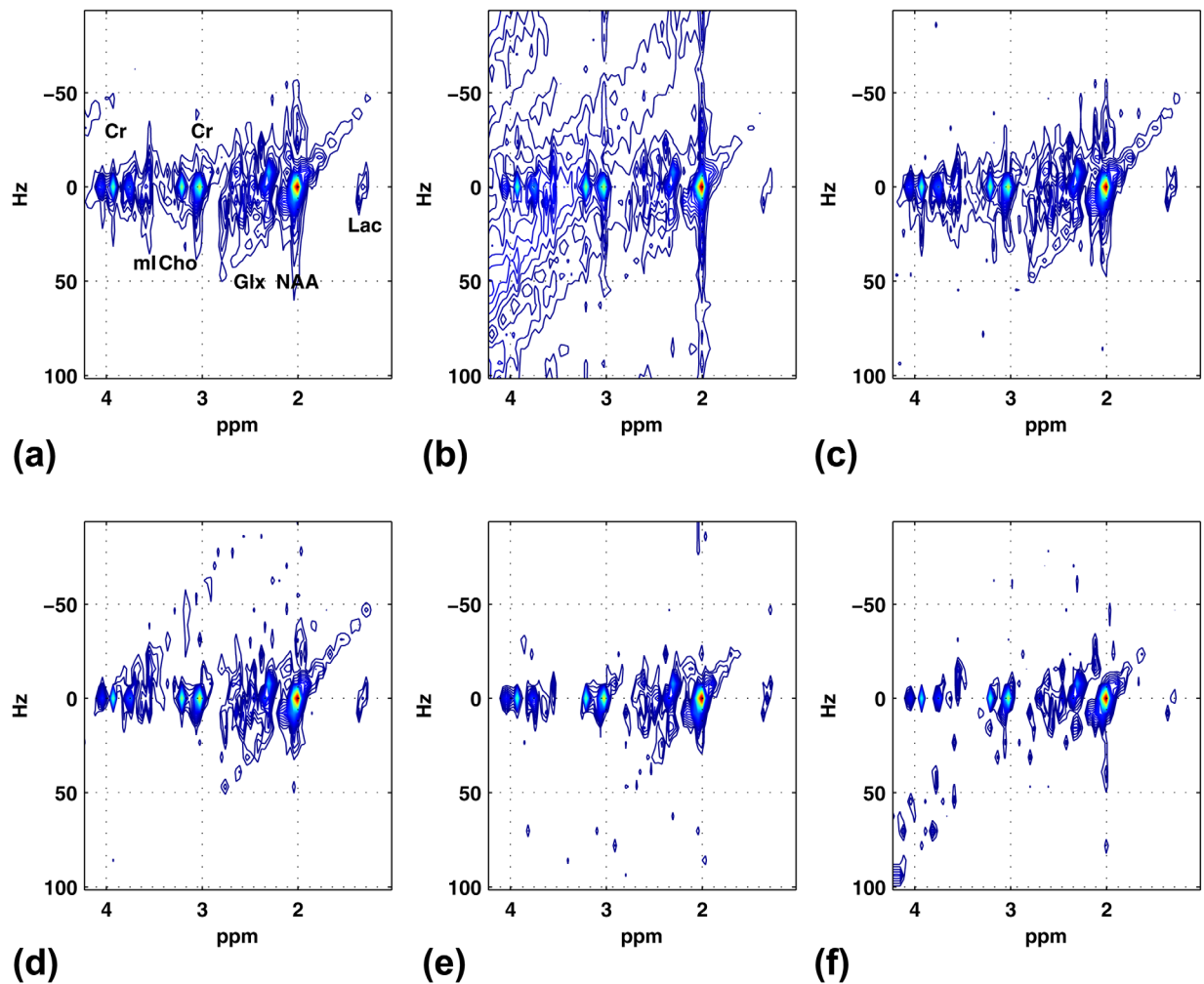


FIG. 2. J-resolved spectrum from the same central voxel in the phantom for different undersampling rates. **a**: fully sampled, **b**: $4\times$ NUS with minimum energy reconstruction (missing data points were filled in with zeros), and **c-f**: ℓ_1 reconstructions for $4\times$, $8\times$, $12\times$, and $16\times$ NUS, respectively.

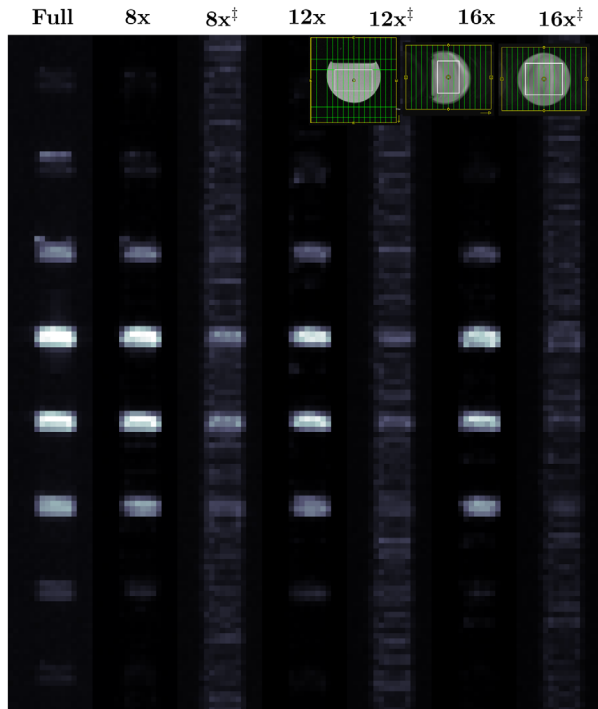


FIG. 3. Glx metabolite map for a typical phantom scan with various retrospective undersamplings. Slices are stacked vertically, and the readout direction is horizontal. Reconstruction was performed according to Eq. (3), minimizing the TV-norm. [†]Reconstruction did not include spectral masking.

undersampling, the reconstructions are shown with and without prior spectral masking as noted. Full spectra from the central voxel of each reconstruction are shown in Figure 4 with the display extended to show the residual water peak. Without spectral masking, the residual water peak is much higher, and the metabolite peaks are reconstructed at lower intensities. Also, comparing Figures 4a–c and 2d–f qualitatively suggests that the TV-norm objective performs better than the ℓ_1 -norm, especially at greater undersampling factors.

Quantitative comparisons between the various undersampling factors and reconstructions over all the phantom scans are shown in Table 2 and Figure 5. In Table 2, peak root-mean-square errors (RMSEs) are computed between the fully sampled and reconstructed data and are reported in decibels (dB). The same spectral region used for peak integration was used for each metabolite RMSE. For proper comparison, the minimum energy reconstructions are also included. Within each reconstruction, there is a clear trend of higher RMSEs with greater undersampling factors for each metabolite. Exceptions occur in the TV reconstruction between 4 \times and 8 \times undersampling and in the ℓ_1 reconstruction of Cr39 between 12 \times and 16 \times . RMSEs are also presented for 8 \times undersampled data reconstructed with ℓ_1 minimization without prior spectral masking. Though the NAA results are surprisingly close to the fully sampled, most of the other metabolites are much less similar and are even worse than the minimum energy reconstruction in some instances, indicating that the spectral mask improves the reconstruction of small to medium peaks. Trends

between the ℓ_1 and TV reconstructions are less obvious with ℓ_1 exhibiting lower RMSEs at lesser undersampling but TV exhibiting lower ones at greater undersampling.

Figure 5 compares the reconstructions by looking at peak integrals of NAA, Glx, Cr, tCho, and mI. In each case, the peak integrals tend to decrease with greater undersampling with the differences being smaller for TV reconstruction. The standard deviations of the fully sampled data are similar to those for each reconstruction, with those of mI being the highest due to its closer proximity to the residual water tail. Supporting Information Table S1 gives the numbers used for this figure.

In Vivo

Due to obvious time constraints, 5D in vivo data was prospectively undersampled only, so there is no fully sampled data to compare with. Quality metrics such as RMSE cannot therefore be calculated. Instead, peak integrals are used to show reproducibility and that values are within the physiological range for healthy adults. Figure 6a shows metabolite maps from a healthy 29-year-old adult using 8 \times undersampling and TV reconstruction. Each metabolite was scaled to its maximum so that they all can appear with the same grey scale despite different overall intensities. Figure 6b shows the full spectra from the voxels highlighted in Figure 6a. The red and blue voxels are from different sides of the occipital lobe, the yellow voxel is from the parietal lobe, and the green voxel is from the frontal lobe. The occipital voxels tend to have the best water suppression and exhibit the highest quality spectra. This is consistent with our previous experience both in single voxel and single slice SI. Fat leakage into the occipital voxels is present but small enough not to disturb the NAA singlet. Voxels in the frontal lobe show worse water suppression due to susceptibility-related effects and difficulties in shimming, and the residual water tail can affect the integrals of the Cr39 singlet and the mI multiplet.

Figure 7 shows the mean metabolite peak integrals over nine healthy adults using TV minimization. Voxels in the frontal lobe (top) were separated from those in the occipital and parietal lobes (bottom). This is because of the markedly increased standard deviations in the frontal lobe in scans with poorer water suppression. A time-equivalent, 4D fully sampled data set is included and shows similar means and standard deviations as the reconstructed 5D data. Supporting Information Figure S2 shows the data reconstructed minimizing the ℓ_1 -norm. Both figures are similar, though the TV reconstruction results in a tighter spread of intersubject averages and slightly smaller intrasubject standard deviations as well. The numeric data for all 10 healthy volunteers along with the number of acceptable voxels for each scan are given in Supporting Information Tables S2 and S3 for voxels in the occipito-parietal and frontal lobes, respectively.

DISCUSSION

The main benefit of the technique described here is the potential for J-resolved SI in three spatial dimensions in vivo. However, the challenges faced in conventional 3D

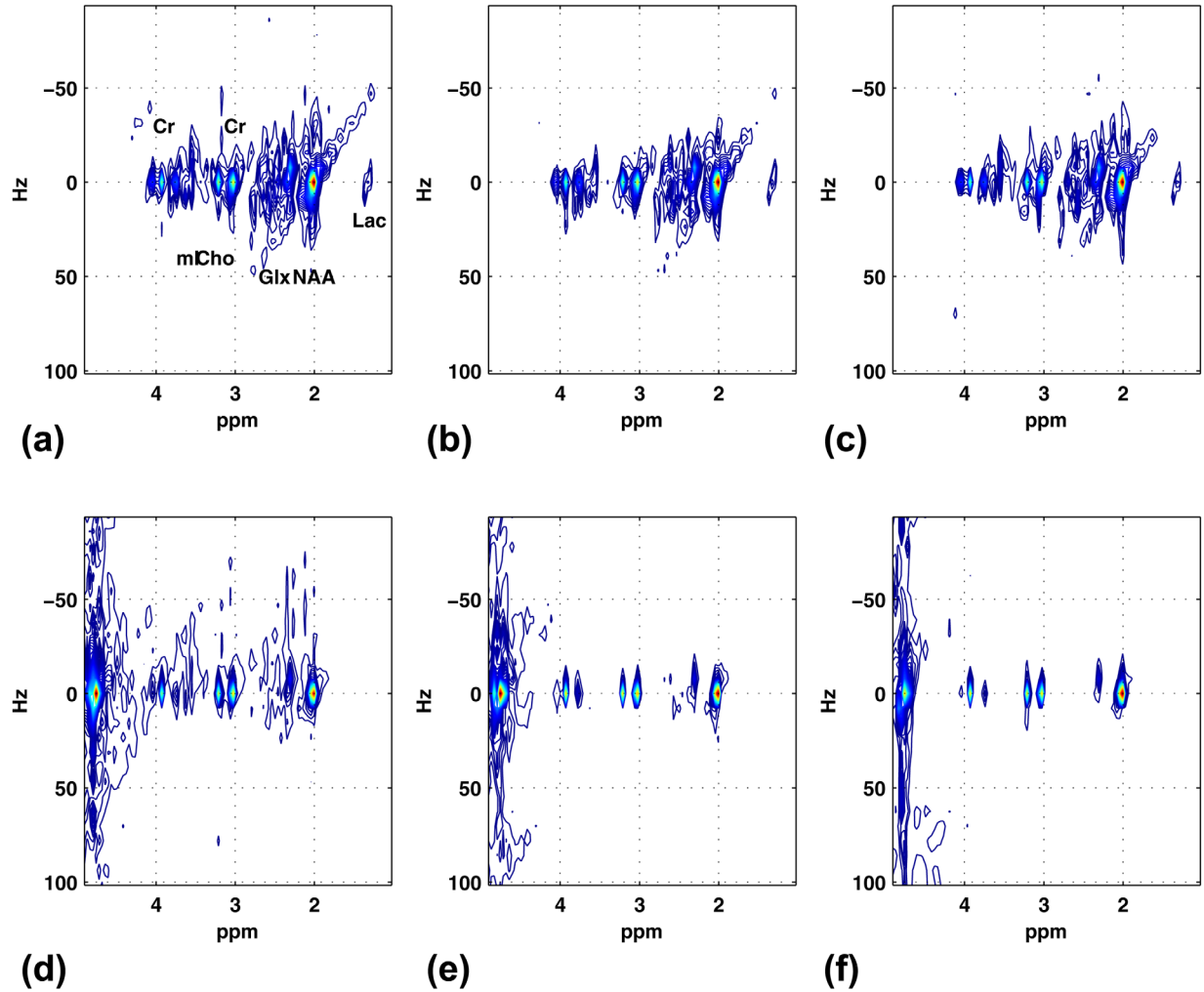


FIG. 4. The effect of spectral masking before reconstruction. J-resolved spectrum from the same central voxel in the phantom for different undersamplings with TV reconstruction. **a–c:** are for $8\times$, $12\times$, and $16\times$ NUS, respectively, and include spectral masking. **d–f:** use the same NUS and reconstruction except without any spectral masking; the contour level has been scaled down by a factor of two to partially compensate for the decreased signal intensity. In all spectra, the F_2 axis is extended to show the residual water peak.

SI are also present here. We have chosen to use a volume-localized (PRESS) echo planar J-resolved SI as opposed to spin echo or slice-localized sequence, despite the better coverage and shorter echo times afforded by the latter. Volume-localized techniques permit better shimming, which leads to taller, narrower peaks suited for CS reconstruction and better water suppression. Also, slice-localized techniques suffer from skull marrow lipid

contamination due to ringing of the high amplitude, low resolution point spread function. Contamination can be partially compensated with inversion recovery (42) or postprocessing techniques involving a high resolution lipid image (43). Outer volume suppression pulses effectively remove all signals (metabolites included) but are difficult to position over the skull marrow in a 3D scan without significantly suppressing cortical signal near the

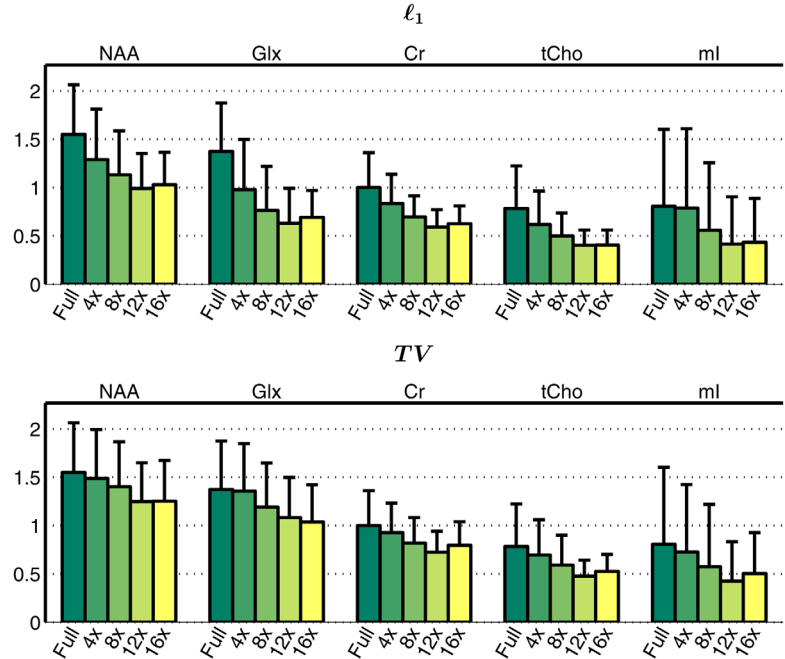
Table 2
Mean Metabolite Peak RMSEs in Phantom in Decibel Scale

	Min En				ℓ_1					TV			
	4 \times	8 \times	12 \times	16 \times	4 \times	8 \times^a	8 \times	12 \times	16 \times	4 \times	8 \times	12 \times	16 \times
NAA	-10.23	-7.22	-5.32	-4.22	-14.71	-14.95	-14.65	-14.53	-14.47	-14.59	-14.67	-14.61	-14.51
Glx	-9.22	-6.64	-4.52	-3.17	-13.98	-6.53	-13.72	-13.67	-13.58	-13.81	-13.67	-13.68	-13.47
Cr30	-9.64	-6.84	-5.10	-3.81	-14.20	-10.74	-14.22	-13.79	-13.76	-14.13	-14.21	-13.99	-13.85
tCho	-9.30	-6.54	-5.08	-3.54	-13.82	-7.09	-13.77	-13.57	-13.41	-13.82	-13.84	-13.68	-13.59
ml	-7.90	-5.78	-4.87	-4.84	-10.96	-4.67	-10.81	-10.72	-10.61	-10.77	-10.49	-10.20	-10.22
Cr39	-9.56	-7.12	-5.50	-4.55	-14.09	-8.03	-13.84	-13.57	-13.71	-14.07	-14.09	-13.81	-13.75

Min En is the minimum energy reconstruction.

^aSpectral masking was not applied prior to reconstruction.

FIG. 5. Peak integrals reconstructed from different undersamplings for five metabolites. Integrals were normalized by the mean of Cr in the fully sampled data. Reconstruction was performed according to Eq. (2) (top) and Eq. (3) (bottom).



surface of the brain. The chosen spectral mask further ensured minimization of any residual lipid artifacts but would be inadequate to remove the ringing caused by unsuppressed signal from the skull marrow by itself.

Volumetric localization using adiabatic RF pulses (44) or adiabatic refocusing pulses (45) can be used to greatly reduce chemical shift displacement error and allow ROIs very near the skull marrow.

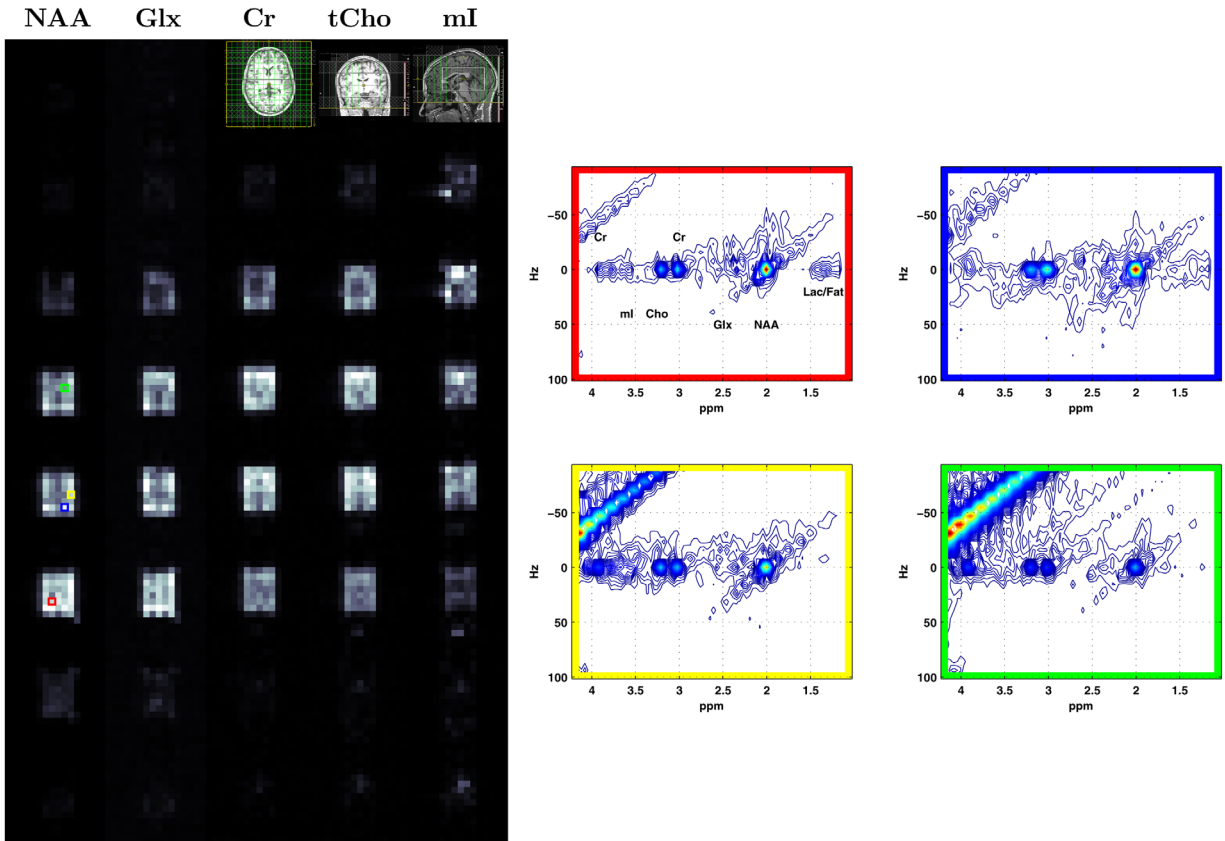


FIG. 6. Metabolites maps (left) for a 29-year-old healthy adult scanned with 8x undersampling and reconstructed using Eq. (3). Each metabolite was normalized to its maximum so that they appear on the same gray scale. Spectra from the highlighted voxels are shown at right.

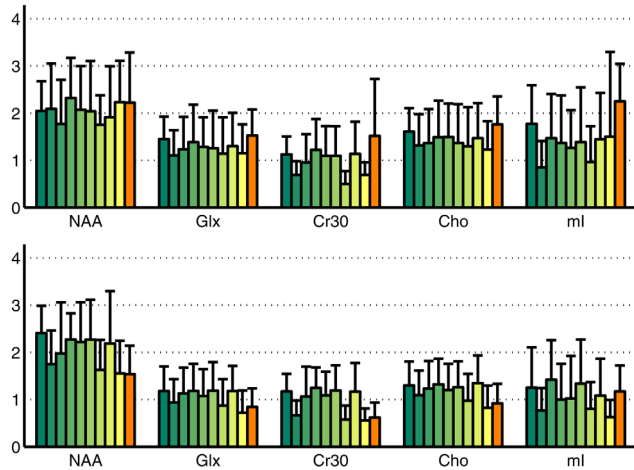


FIG. 7. Regional peak integrals of major metabolites in ten healthy adults with minimum TV reconstruction. The green bars are from $8\times$ NUS 5D data reconstructed using Eq. (3) for voxels in the frontal lobe (top) and in the occipito-parietal lobes (bottom). The orange bar is from a time-equivalent, fully sampled 4D data set for comparison.

maps in Figure 6a, there is about a one pixel shift per ppm in the y -direction and a $1/2$ slice shift per ppm using the “Mao” refocusing pulses (46) in PRESS.

In this work, we have used two methods for quantitative comparison of reconstructed data. The RMSE is applicable when a reference signal is available as was the case with phantom data only. It is a point-by-point method, and as such, it is sensitive to differences in amplitude, linewidth, and peak shape. However, it is also influenced by noise and can be biased by the nonlinear reconstruction methods used here. To minimize the influence of noise and better characterize where discrepancies are occurring, RMSEs were constrained to the individual metabolite peak areas. As an additional quantitative method, peak integration simply sums the volume in a given region and therefore does not directly describe differences in amplitude, linewidth, or peak shape. No reference data is required, but over- or underestimation can be determined if it is present. From a philosophical standpoint, peak integration provides a relative measure of metabolite concentration which is the penultimate goal in spectroscopy studies anyway. Both methods can be considered complementary.

The decrease in peak volumes from fully sampled to $12\times$ undersampling shown in Figure 5 is consistent with the corresponding increase in RMSE values shown in Table 2 and is most likely the result of the nonlinear reconstruction itself. In either ℓ_1 or TV minimization, soft thresholding tends to shrink the amplitudes of the signal in the transform domain (identity or finite differences), reducing the peak integral. The data consistency term is what mitigates this effect. However, the larger the undersampling factor, the less influence the data consistency term has (assuming that the value of σ does not depend on R). Simply put, there are fewer data points to constrain.

Previous work on CS-reconstructed single slice J-resolved SI data has suggested that TV reconstruction

should perform better than ℓ_1 (23). In this case though, adding a third spatial dimension increases the self sparsity of the data as the ROI is about half the FOV in the z -direction, and several slices do not contribute any signal. This effectively narrows the gap between the reconstructions to the point that it is not definitive if there is a significant difference. The reconstruction in Eq. (2) takes about 10 min per coil, while that of Eq. (3) takes about half an hour on a 64-bit octa core 3.1 GHz Intel Xeon E5-2687W processor with 128 GB RAM, so there is strong incentive to choose the faster reconstruction method when the number of coils is large. Coil compression methods could be applied to the acquired data to reduce the number of virtual coils that need to be reconstructed (47). It should be noted that a scan with a tighter FOV around the volume of interest would be less self sparse though and could negatively influence the ℓ_1 reconstruction. However, the TV reconstruction should be relatively immune to the ROI/FOV ratio as long as the object profile is not wildly varying.

A relatively large indirect spectral bandwidth of 500 Hz was used in this article. Often, J-resolved spectra can be acquired with a bandwidth less than 100 Hz due to the small coupling constants found in most metabolites (32). The primary reason for this choice was to keep the residual water tail away from the metabolite signals, as we have found it difficult to achieve consistent water suppression over the whole brain. A further consequence of this choice is that the 2D spectra are highly sparse, which benefits the reconstruction. However, a large indirect spectral bandwidth is not a prerequisite for the technique described. The same principles of sampling (Eq. (1)) and reconstruction can be applied with minimal modification to low indirect bandwidth data with the similar caveat that the ℓ_1 reconstruction will be more negatively affected than the TV.

Figures 3 and 4 show how important a simple spectral masking is prior to the reconstruction. In either reconstruction, the data fidelity term will make sure the largest peaks are reconstructed most accurately, while low-lying peaks are “cleaned up” as aliasing and largely removed. Even with good water suppression, the residual water is typically the largest peak in brain spectra. Individual peaks of multiplets are smaller and reconstructed with much less intensity as shown in the above mentioned figures. Conversely, the NAA singlet peak has the second highest amplitude and is well separated from the residual water tail. It is reconstructed accurately with or without masking in Table 2, but the errors in reconstruction for Glx and ml are much more pronounced. As an alternative to the simple spectral masking presented here, other postprocessing methods to remove the residual water signal can be applied instead, for instance that based on wavelet transformation (48). This method would be advantageous when requiring accurate quantitation of metabolites very near the water peak, such as glutathione. The same idea applies to the lipid peaks and their effect on lactate and alanine.

Table 2 and Figure 4 suggest that undersampling factors up to $16\times$ can be achieved with excellent reconstruction quality in phantom. However, we have limited ourselves to $8\times$ undersampling in vivo. The reason for

this conservative choice is in consideration of the motivation to do multidimensional spectroscopy in the first place. The major singlet resonances in brain are well resolved in single dimensional spectroscopy with long echo times. The advantage of using multidimensional spectroscopy lies in its ability to resolve low amplitude, J -coupled resonances acquired with short echo times. Without accurate measurements of these additional resonances, there is no reason not to choose the much faster 1D technique. As the undersampling factor increases, more of the low amplitude resonances are buried in the noise and residual aliasing and will not be reconstructed accurately. Future work will look at prior knowledge fitting as an improved method of quantification of up to 20 brain metabolites (49).

Further improvements may be made by considering additional NUS schemes and reconstruction objectives. In particular, the Poisson gap sampling scheme shows reduced artifacts compared to random undersampling (50). Maximum entropy has been used as an objective in 2D NMR and might offer some improvement compared to ℓ_1 -norm minimization (51,52), while group sparsity uses the $\ell_{2,1}$ -norm objective to consider the proximity of nonzero coefficients (53).

Although this article has focused on 2D J -resolved spectroscopy, the techniques can be applied with suitable modification to imaging analogs of other 2D acquisitions such as correlated spectroscopy, TE-averaged PRESS (54), or CT-PRESS (55). Despite the common practice of displaying the latter two as single dimension spectra, the acquisition requires two spectral dimensions and can be undersampled and reconstructed as 2D spectra with the methods described here before taking the appropriate projections.

CONCLUSION

NUS with CS reconstruction can be used to acquire 5D (3 spatial + 2 spectral) spectroscopic images in human brain in a clinically feasible scan time. Conservatively, an 8-fold acceleration was applied in vivo for a 20 minute scan time, while a 16-fold acceleration was applied to phantom data. Reconstruction can be performed either by minimizing the ℓ_1 -norm or the TV-norm.

ACKNOWLEDGMENTS

The authors thank Dr. Paul Macey for the purchase of a high performance workstation, Dr. Jon Furuyama for fruitful discussions during the early phase of this project, and Ms. Judy Hayes for subject recruitment.

REFERENCES

- Brown TR, Kincaid BM, Ugurbil K. NMR chemical shift imaging in three dimensions. *Proc Natl Acad Sci* 1982;79:3523–3526.
- Mansfield P. Spatial mapping of the chemical shift in NMR. *J Phys D Appl Phys* 1983;16:L235–L238.
- Posse S, Tedeschi G, Risinger R, Ogg R, Bihan DL. High speed 1H spectroscopic imaging in human brain by echo planar spatial-spectral encoding. *Magn Reson Med* 1995;33:34–40.
- Adalsteinsson E, Irrazabal P, Topp S, Meyer C, Macovski A, Spielman DM. Volumetric spectroscopic imaging with spiral-based k-space trajectories. *Magn Reson Med* 1998;39:889–898.
- Furuyama JK, Wilson NE, Thomas MA. Spectroscopic imaging using concentric circular echo-planar trajectories in vivo. *Magn Reson Med* 2012;67:1515–1522.
- Aue WP, Bartholdi E, Ernst RR. Twodimensional spectroscopy. Application to nuclear magnetic resonance. *J Chem Phys* 1976;64:2229–2246.
- Ryner LN, Sorenson JA, Thomas M. Localized 2D J -resolved 1H MR spectroscopy: strong coupling effects in vitro and in vivo. *Magn Reson Imaging* 1995;13:853–869.
- Thomas MA, Yue K, Binesh N, et al. Localized two-dimensional shift correlated MR spectroscopy of human brain. *Magn Reson Med* 2001;46:58–67.
- Andronesi OC, Ramadan S, Mountford CE, Sorensen A. Low-power adiabatic sequences for in vivo localized two-dimensional chemical shift correlated MR spectroscopy. *Magn Reson Med* 2010;64:1542–1556.
- Bottomley PA. Spatial localization in NMR spectroscopy in vivo. *Ann N Y Acad Sci* 1987;508:333–348.
- Adalsteinsson E, Spielman DM. Spatially resolved two-dimensional spectroscopy. *Magn Reson Med* 1999;41:8–12.
- Lipnick S, Verma G, Ramadan S, Furuyama J, Thomas MA. Echo planar correlated spectroscopic imaging: implementation and pilot evaluation in human calf in vivo. *Magn Reson Med* 2010;64:947–956.
- Andronesi OC, Gagoski BA, Adalsteinsson E, Sorensen AG. Correlation chemical shift imaging with low-power adiabatic pulses and constant-density spiral trajectories. *NMR Biomed* 2012;25:195–209.
- MacFall JR, Pelc NJ, Vavrek RM. Correction of spatially dependent phase shifts for partial Fourier imaging. *Magn Reson Imaging* 1988;6:143–155.
- Pruessmann KP, Weiger M, Scheidegger MB, Boesiger P. SENSE: sensitivity encoding for fast MRI. *Magn Reson Med* 1999;42:952–962.
- Griswold MA, Jakob PM, Heidemann RM, Nittka M, Jellus V, Wang J, Kiefer B, Haase A. Generalized autocalibrating partially parallel acquisitions (GRAPPA). *Magn Reson Med* 2002;47:1202–1210.
- Maudsley AA, Matson GB, Hugg JW, Weiner MW. Reduced phase encoding in spectroscopic imaging. *Magn Reson Med* 1994;31:645–651.
- Dydak U, Weiger M, Pruessmann KP, Meier D, Boesiger P. Sensitivity-encoded spectroscopic imaging. *Magn Reson Med* 2001;46:713–722.
- Lin FH, Tsai SY, Otazo R, Caprihan A, Wald LL, Belliveau JW, Posse S. Sensitivity-encoded (SENSE) proton echo-planar spectroscopic imaging (PEPSI) in the human brain. *Magn Reson Med* 2007;57:249–257.
- Otazo R, Tsai SY, Lin FH, Posse S. Accelerated short-TE 3D proton echo-planar spectroscopic imaging using 2D-SENSE with a 32-channel array coil. *Magn Reson Med* 2007;58:1107–1116.
- Lustig M, Donoho D, Pauly JM. Sparse MRI: the application of compressed sensing for rapid MR imaging. *Magn Reson Med* 2007;58:1182–1195.
- Hu S, Lustig M, Chen AP, et al. Compressed sensing for resolution enhancement of hyperpolarized ^{13}C flyback 3D-MRSI. *J Magn Reson* 2008;192:258–264.
- Furuyama JK, Wilson NE, Burns BL, Nagarajan R, Margolis DJ, Thomas MA. Application of compressed sensing to multidimensional spectroscopic imaging in human prostate. *Magn Reson Med* 2012;67:1499–1505.
- Roy B, Gupta R, Maudsley A, et al. Utility of multiparametric 3-T MRI for glioma characterization. *Neuroradiology* 2013;55:603–613.
- Govind V, Gold S, Kaliannan K, Saigal G, Falcone S, Arheart KL, Harris L, Jagid J, Maudsley AA. Whole-brain proton MR spectroscopic imaging of mild-to-moderate traumatic brain injury and correlation with neuropsychological deficits. *J Neurotrauma* 2010;27:483–496.
- Stagg CJ, Knight S, Talbot K, Jenkinson M, Maudsley AA, Turner MR. Whole-brain magnetic resonance spectroscopic imaging measures are related to disability in ALS. *Neurology* 2013;80:610–615.
- Verma G, Woo JH, Chawla S, et al. Whole-brain analysis of amyotrophic lateral sclerosis by using echo-planar spectroscopic imaging. *Radiology* 2013;267:851–857. PMID: 23360740.
- Gu M, Kim DH, Mayer D, Sullivan EV, Pfefferbaum A, Spielman DM. Reproducibility study of whole-brain 1H spectroscopic imaging with automated quantification. *Magn Reson Med* 2008;60:542–547.
- Maudsley A, Domenig C, Govind V, Darkazanli A, Studholme C, Arheart K, Bloomer C. Mapping of brain metabolite distributions by volumetric proton MR spectroscopic imaging (MRSI). *Magn Reson Med* 2009;61:548–559.

30. Dreher W, Erhard P, Leibfritz D. Fast three-dimensional proton spectroscopic imaging of the human brain at 3 T by combining spectroscopic missing pulse steady-state free precession and echo planar spectroscopic imaging. *Magn Reson Med* 2011;66:1518–1525.
31. Ding XQ, Maudsley AA, Sabati M, Sheriff S, Dellani PR, Lanfermann H. Reproducibility and reliability of short-TE whole-brain MR spectroscopic imaging of human brain at 3T. *Magn Reson Med* 2014, March 26 [Epub ahead of print].
32. Govindaraju V, Young K, Maudsley AA. Proton NMR chemical shifts and coupling constants for brain metabolites. *NMR Biomed* 2000;13:129–153.
33. Macura S, Brown LR. Improved sensitivity and resolution in two-dimensional homonuclear J-resolved NMR spectroscopy of macromolecules. *J Magn Reson* 1983;53:529–535.
34. Schulte RF, Lange T, Beck J, Meier D, Boesiger P. Improved two-dimensional J-resolved spectroscopy. *NMR Biomed* 2006;19:264–270.
35. Ogg R, Kingsley R, Taylor J. WET, a T1- and B1-insensitive water-suppression method for in vivo localized 1H NMR spectroscopy. *J Magn Reson, Ser B* 1994;104:1–10.
36. Barna J, Laue E, Mayger M, Skilling J, Worrall S. Exponential sampling, an alternative method for sampling in two-dimensional NMR experiments. *J Magn Reson* 1987;73:69–77.
37. Goldstein T, Osher S. The split Bregman method for L1 regularized problems. *SIAM J Imaging Sci* 2009;2:323–343.
38. Bertsekas DP. Multiplier methods: a survey. *Automatica* 1976;12:133–145.
39. Esser E. Applications of Lagrangian-based alternating direction methods and connections to split Bregman. *CAM Rep* 2009;9:31.
40. Eslami R, Jacob M. Robust reconstruction of MRSI data using a sparse spectral model and high resolution MRI priors. *IEEE Trans Med Imaging* 2010;29:1297–1309.
41. Gudbjartsson H, Patz S. The rician distribution of noisy MRI data. *Magn Reson Med* 1995;34:910–914.
42. Spielman DM, Pauly JM, Macovski A, Glover GH, Enzmann DR. Lipid-suppressed single-and multisection proton spectroscopic imaging of the human brain. *J Magn Reson Imaging* 1992;2:253–262.
43. Haupt CI, Schuff N, Weiner MW, Maudsley AA. Removal of lipid artifacts in 1H spectroscopic imaging by data extrapolation. *Magn Reson Med* 1996;35:678–687.
44. Garwood M, DelaBarre L. The return of the frequency sweep: designing adiabatic pulses for contemporary NMR. *J Magn Reson* 2001;153:155–177.
45. Scheenen TWJ, Klomp DWJ, Wijnen JP, Heerschap A. Short echo time 1H-MRSI of the human brain at 3T with minimal chemical shift displacement errors using adiabatic refocusing pulses. *Magn Reson Med* 2008;59:1–6.
46. Mao J, Mareci T, Andrew E. Experimental study of optimal selective 180 radiofrequency pulses. *J Magn Reson* 1988;79:1–10.
47. Buehrer M, Pruessmann KP, Boesiger P, Kozerke S. Array compression for MRI with large coil arrays. *Magn Reson Med* 2007;57:1131–1139.
48. Günther UL, Ludwig C, Rüterjans H. WAVEWAT-improved solvent suppression in NMR spectra employing wavelet transforms. *J Magn Reson* 2002;156:19–25.
49. Schulte RF, Boesiger P. ProFit: two-dimensional prior-knowledge fitting of J-resolved spectra. *NMR Biomed* 2006;19:255–263.
50. Hyberts SG, Takeuchi K, Wagner G. Poisson-gap sampling and forward maximum entropy reconstruction for enhancing the resolution and sensitivity of protein NMR data. *J Am Chem Soc* 2010;132:2145–2147. PMID: 20121194.
51. Stern AS, Donoho DL, Hoch JC. NMR data processing using iterative thresholding and minimum l1-norm reconstruction. *J Magn Reson* 2007;188:295–300.
52. Burns B, Wilson NE, Furuyama JK, Thomas MA. Non-uniformly under-sampled multi-dimensional spectroscopic imaging in vivo: maximum entropy versus compressed sensing reconstruction. *NMR Biomed* 2014;27:191–201.
53. Burns BL, Wilson NE, Thomas MA. Group sparse reconstruction of multi-dimensional spectroscopic imaging in human brain in vivo. *Algorithms* 2014;7:276–294.
54. Hurd R, Sailasuta N, Srinivasan R, Vigneron DB, Pelletier D, Nelson SJ. Measurement of brain glutamate using TE-averaged PRESS at 3T. *Magn Reson Med* 2004;51:435–440.
55. Dreher W, Leibfritz D. Detection of homonuclear decoupled in vivo proton NMR spectra using constant time chemical shift encoding: CT-PRESS. *Magn Reson Imaging* 1999;17:141–150.

SUPPORTING INFORMATION

Additional Supporting Information may be found in the online version of this article.

Supporting Figure S1: Localized three plane image of phantom (left) and NAA metabolite map for a typical phantom scan with various retrospective undersamplings (right). The phase encoding direction is shown vertically, the readout is horizontal, and the slices are stacked. Reconstruction was performed according to Eq. (2), minimizing the '1-norm except where noted. †Minimum energy reconstruction.

Supporting Figure S2: Regional peak integrals of major metabolites in ten healthy adults with minimum '1 reconstruction. The green bars are from 8x NUS 5D data reconstructed using Eq. (2) for voxels in the frontal lobe (top) and in the occipito-parietal lobes (bottom). The orange bar is from a time-equivalent, fully-sampled 4D data set for comparison.

Supporting Table S1: Mean metabolite peak integrals in phantom with standard deviations in parentheses.

Supporting Table S2: Mean metabolite peak integrals from the occipito-parietal lobes in vivo of 10 healthy volunteers. Standard deviations are in parentheses, and the number of included voxels are given for each scan. The top half shows the reconstruction minimizing the '1-norm, while the bottom half is the result from minimizing the T V -norm. The last column shows the values from a fully sampled single slice (4D) scan.

Supporting Table S3: Same as Supporting Table S2 for voxels in the frontal lobe.